Title

Bottlebrush Polymers at Liquid Interfaces: Assembly Dynamics, Mechanical Properties, and All-Liquid Printed Constructs

Journal

ACS Nano, 17(15)

ISSN

1936-0851

Authors

Seong, Hong-Gyu

Fink, Zachary

Chen, Zhan

et al.

Publication Date

2023-08-08

DOI

10.1021/acsnano.3c02684

Bottlebrush Polymers at Liquid Interfaces: Assembly Dynamics, Mechanical Properties, and All-Liquids Printed Constructs

Hong-Gyu Seong[1], *Zachary Fink*[1,2], *Zhan Chen*[1], *Todd Emrick*[1]* *and Thomas P. Russell*[1,2]*

[1]Polymer Science and Engineering Department, Conte Center for Polymer Research, University of Massachusetts, 120 Governors Drive, Amherst, MA 01003 (USA)

[2]Materials Sciences Division, Lawrence Berkeley National Laboratory, 1 Cyclotron Road, Berkeley, CA 94720 (USA)

*Corresponding authors E-mail: tsemrick@mail.pse.umass.edu; russell@mail.pse.umass.edu

Bottlebrush polymer surfactants / Soft nanoparticles / Jamming / Structure-property relationship / All-liquids printed constructs

ABSTRACT.

Bottlebrush polymers (BPs) with poly(acrylic acid) sidechains were found to assemble and bind strongly at fluid interfaces by the formation of *bottlebrush polymer surfactants* (BPSs), where carboxylic acids of BPs dispersed in water interact with ligands having complementary functional groups, primary amines, dissolved in toluene. The ratio between N_{BB} (degree of polymerization of the backbone) and N_{SC} (degree of polymerization of the sidechain) was found to affect the initial assembly kinetics, interface packing efficiency, and stress relaxation behavior. The equilibrium interfacial tension (γ) increased when $N_{BB}<N_{SC}$, but decreased when $N_{BB}>>N_{SC}$, which correlates with the change of the macromolecular topology (a rigid cylinder to a semi-flexible worm-like macromolecule, respectively). The apparent surface coverage (ASC), which characterizes the efficiency of packing at fluid interfaces, was found to decrease as N_{BB} increased. Both continuous injection of polymer solution (related to suppressing Plateau-Rayleigh instability) and fluorescence recovery after photobleaching experiments revealed a more rapid initial assembly kinetics for higher N_{BB} BPs. Euler buckling of BPSs with different N_{BB} was used to quantify the stress relaxation behavior and bending modulus of BPSs. The stress relaxation behavior was found to be directly related to the ASC, reflecting the importance of macromolecular topology on packing efficiency. The bending modulus of BPSs found to decrease for $N_{BB}<N_{SC}$, but increased for

N_{BB}>>N_{SC}, showing the effect of molecular topology as well as the multi-site anchoring nature of BPs in this regime. All-liquid printed constructs with different N_{BB} showed that lower N_{BB} BPs yielded more stable structured liquids, underscoring the importance of the packing efficiency of macromolecules at fluid interfaces. This work elucidates fundamental nanoscopic structure-macroscopic property relationships associated with the N_{BB}~N_{SC} ratio, which can be used in the use of structured liquids generated by BPSs.

INTRODUCTION.

Even after Pickering showed the potential utility of solid particles (nano- to micrometer) as emulsifiers, relatively little attention was given to this remarkable finding.[1] Several decades later, with precise control over the size and dispersity of colloidal and nanoparticles, the field of emulsions stabilized by solid particles has expanded significantly.[2, 3] Pieranski, for example, showed that polystyrene nanoparticles (PS NPs, ~250 nm in diameter) stabilized the water-air interface and, due to dipolar repulsive interactions, formed 2D crystalline arrays at the interface.[4] Subsequently, Pickering emulsion systems from particles of different composition, sizes, and surface chemistries have been developed.[5] Since the decrease in the interfacial energy per particle is proportional to the particle cross section, *i.e.,* square of the diameter, as particle size decreases from colloidal (micron) to nanoscale, the binding energy or energy gain in placing a particle at the interface decreases by several orders of magnitude, becoming comparable to thermal energy, several k_BT, where k_B is the Botlzmann constant, and T is the temperature in degrees Kelvin.[4] Consequently, interfacially bound nanoparticles (NPs) are easily ejected from the interface of immiscible fluids as the system reduces the interfacial area to minimize the free energy, and spherical domains of one liquid dispersed in a second liquid are found.[6]

The binding energy of NPs at fluid interfaces can be markedly enhanced by the formation of *nanoparticle surfactants (NPSs)*, where surface-functionalized NPs dispersed in one liquid interact with ligands having complementary functionality dissolved in a second immiscible liquid (*e.g.*, carboxylate-functionalized NPs in water and amine functionalized oligomers dissolved in organic solvent).[7] The ligands will non-covalently anchor to the NPs to maximize the gain in the free energy per particle when placed at the interface to form the NPSs. This massively increases the binding energy of each NP to the interface, such that as the interfacial area is decreased to minimize the interfacial free energy, the compressive force exerted on the particles is

not sufficient to displace them. As a result, the interfacial assembly of NPSs jams, locking in non-equilibrium shapes of the liquid. Further external compression will cause the NPS assembly to wrinkle (*i.e.*, Euler buckling), where the wavelength of the wrinkle pattern is related directly to the bending modulus of the assembly.[8] NPSs containing NPs of different dimensionality have been investigated, including 0D (spherical inorganic[7], polymeric[9], metallic[10] or organic, *e.g.*, polyhedral oligomeric silsequioxane NPs[11]), 1D (single-walled carbon nanotubes[12], nanorods[13], cellulose nanocrystals[14], and bottlebrush polymers[15]), and 2D (graphene oxide[16], MXene[17] and transition metal dichalcogenides[18]) NPs interacting with ligands or oligomers electrostatically[19], through complexation chemistries[20], host-guest interactions[21], intermolecular π-stacking[22], and redox-responsive systems[23].

Recent developments in controlled radical and ionic (cationic and anionic) polymerization techniques have led to the synthesis of polymer surfactants with controlled topologies, *i.e.,* spherical, cylindrical, discoidal and toroidal.[24, 25] Matyjaszewski and coworkers described the 'surfactancy' of star/bottlebrush copolymers prepared by orthogonal protection-deprotection assisted atom-transfer radical polymerization (ATRP) as a function of composition (hydrophilic-hydrophobic ratio), concentration, and length of both side chains and backbone.[26] Müller and coworkers developed a route to Janus polymer NPs with different geometries (*e.g.*, spheres, cylinders, discs and rings), and described their dynamic interfacial assembly behavior.[27] We have investigated the jamming behavior of spherical polymer-based Janus NPs[28], and the assembly dynamics of bottlebrush random copolymers at fluid interfaces as a function of degree of polymerization of backbone (N_{BB}) and, hence, topologies (spherical for lower N_{BB} and cylindrical for higher N_{BB}).[29] In addition to the above examples, bottlebrush homopolymers containing poly(acrylic acid) sidechains were also prepared as soft nanoparticles (SNPs), that wrinkled upon reduction of interfacial area, demonstrating that cylindrical bottlebrush polymers can bind strongly to fluid interfaces and form elastic films.[15] This jamming behavior make bottlebrush polymers confined to liquid interfaces an ideal platform for the preparation of "*structured liquids*". However, the influence of the bottlebrush architecture on dynamics and mechanical properties is unusual, given the limited penetration between adjacent chains due to the crowding of chains around each backbone[30] that, in the bulk, gives rise to rapid kinetics and dynamics, as the lineal density of chains along the backbone increases.[31] This limited

interpenetration of adjacent chains markedly reduces inter-chain entanglements. While reports describe these parameters in the bulk, they are absent for bottlebrushes confined to fluid interfaces.

Produced by 3D printing or molding, structured liquids have become a versatile platform for directing fluid flow or compartmentalizing fluids while enabling functionalization of the walls confining the fluid.[32] The marked reduction in the interfacial energy due to the formation and assembly of the NPSs at the interface overcomes Plateau-Rayleigh instabilities allowing one fluid to be jetted into a second fluid, while the reduction in the interfacial area of the jetted fluid causes a jamming of NPS assemblies, kinetically trapping the non-equilibrium shape of the printed tubule.[33, 34] This requires the NPSs assembly to form rapidly, the binding energy of the NPSs to be high enough to withstand the lateral stress exerted by the compression of the assembly, and the mechanical properties of elastic film formed by NPSs to be robust enough to maintain the printed liquid structure.[32] Bottlebrush polymers are particularly attractive in this regard, since the high lineal density of the pendant polymer chains attached to the backbone chain afford a high density of functional groups that can be used to interact with oligomers having a complementary functionality dissolved in a second immiscible liquid at the interface to form *bottlebrush polymer surfactants* (BPSs) or for the placement of specific functionality to react with materials contained within or flowing through the structured liquid (**Scheme 1**). To successfully print with bottlebrush polymers, fundamental questions regarding the assembly kinetics, equilibrium packing density, and the mechanical properties of the BPSs must be elucidated.

Here, we describe the preparation of bottlebrush polymers to investigate the dependence of N_{BB} on the assembly, packing dynamics, and packing densities (when $\Delta\gamma/\Delta t \sim 0$) at fluid interfaces. We find that the molecular topologies dictated by the N_{BB}~N_{SC} (degree of polymerization of sidechains) ratio is critical to their nanoscopic assembly, which in turn affords macroscopic stability to the all-liquid printed constructs. This work describes fundamental assembly behavior (both initial and equilibrium stages) and rational design rules for the use of bottlebrush polymers for the 3D printing of structured liquids.

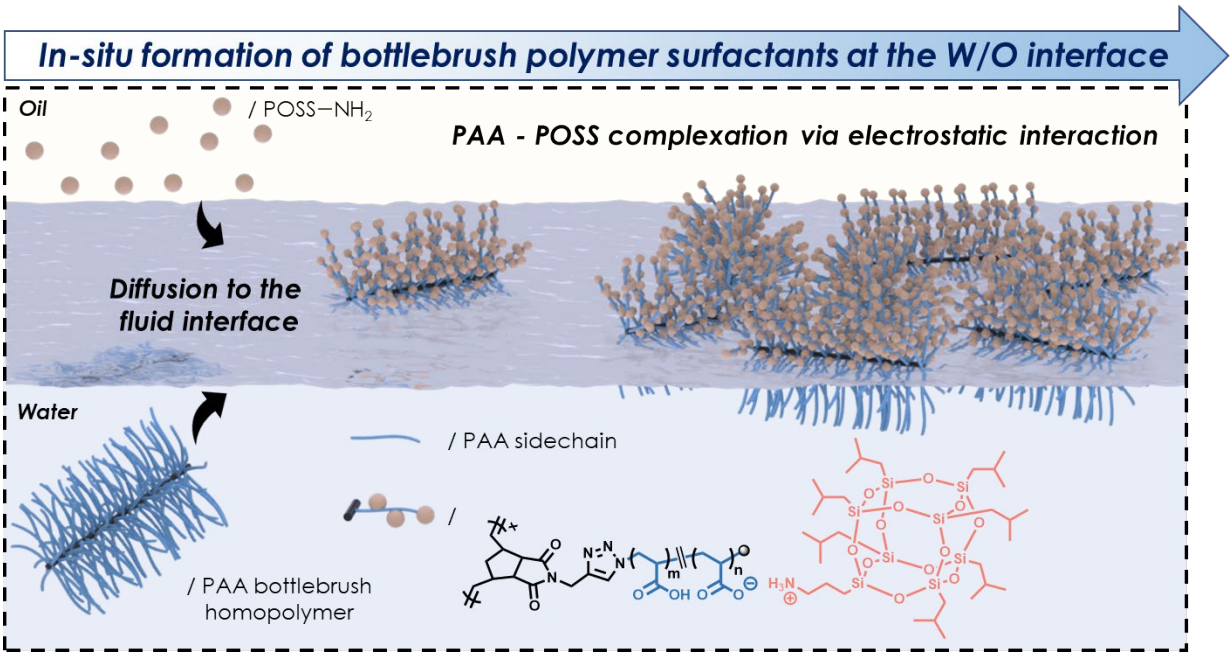

Scheme 1. Schematic illustration of formation of bottlebrush polymer surfactants at the water/oil interface via carboxylate (poly(acrylic acid))-ammonium (polyhedral silsequioxane-NH_2, POSS-NH_2) electrostatic interaction.

RESULTS AND DISCUSSION

ROMP of Poly(acrylic acid) Bottlebrush Homopolymers

Atom-transfer radical polymerization was performed to synthesize a bromine-terminated poly(*tert*-butyl acrylate) (**P*t*BA-Br**) with addition of $Cu^{II}Br_2$ (5 molar % compared to $Cu^{I}Br$) to reduce the concentration of activated radical chain ends. The polymerization was quenched at ~80% conversion to avoid complications from bimolecular coupling ($M_{n,\,GPC}$ ~ 5.4 kDa, PDI = 1.07, **Figures S3, 4**). Then nucleophilic substitution of the ω-bromine chain-ends with NaN_3 yielded **P*t*BA-N_3** with quantitative conversion, as characterized by nuclear magnetic resonance (NMR) spectroscopy (**Figures S5, 6**). Copper-catalyzed alkyne-azide cycloaddition (CuAAC) of P*t*BA-N_3 with *N*-(propargyl)-*cis*-5-norbornene-*exo*-2,3-dicarboximide (prepared from *cis*-5-norbornene-*exo*-2,3-dicarboxylic anhydride and propargyl amine[35]) yielded the desired poly (*tert*-butyl acrylate) macromonomer (**P*t*BA-MM**, $M_{n,\,GPC}$ ~ 5.0 kDa, PDI = 1.07, **Figures S7**, **8**, and **17**). ^{1}H NMR spectroscopy was used to quantify the degree of ω-chain-end functionalization, by integration of the vinyl protons of norbornene dicarboxyimide (ω-chain-ends, 2H at 6.26 ppm) against the methylene protons of the ATRP initiator (α-chain-ends, 2H at 4.09 ppm). The results indicated that ~92% of P*t*BA chain ends were functionalized with norbornene dicarboxyimide.

Figure 1a illustrates the synthesis of poly(acrylic acid) bottlebrush polymers (PAA-BPs), where P*t*BA bottlebrush polymers with different N_{BB} values (**P1**-**P5**) were prepared by ruthenium benzylidene-initiated ring-opening metathesis polymerization (ROMP) of the **P*t*BA-MM**, by tuning the [**P*t*BA-MM**]:[**initiator**] feed ratio. The molecular weights of the polymers with different N_{BB} were characterized by multi-angle laser light scattering assisted size-exclusion chromatography (MALLS-SEC). As the [macromonomer]:[initiator] feed ratio increased, the elution profiles shifted to the shorter times, demonstrating successful molecular weight (MW) control (**Figure 1b**) with high macromonomer conversion (~95 %). The MW of each N_{BB} polymer was close to the predicted MW (black diagonal line, **Figure 1c**). Characterization data for the synthesized P*t*BA-bottlebrush polymers (P*t*BA-BPs) are summarized in **Figure 1c** and **Table 1**. The number-average molecular weight (M_n) of the polymers were in the 90-2,400 kDa range, with polydispersity index (PDI) values of ~1.2-1.3. Following the acid-catalyzed hydrolysis of the *tert*-butyl group, PAA-BPs precipitated during the hydrolysis reaction performed in dichloromethane (DCM) to yield a white powder. Subsequent washing with DCM (3x30 mL) yielded the final PAA bottlebrush polymers (**PD1**-**PD5**) in ~95% yield. Attenuated total reflection Fourier-transform infrared spectroscopy (ATR FT-IR) was used to monitor the hydrolysis reaction, noting the appearance of a broad -OH stretch from 3,500-3,000 cm^{-1} and a shift of the carbonyl (C=O) peak from the ester (1,723 cm^{-1}) to carboxylic acid (1,700 cm^{-1}) (**Figure S19**). The MWs of the PAA-BPs were determined by subtracting the MW of *tert*-butyl groups of P*t*BA-BPs from their original MWs and are summarized in **Table S1**.

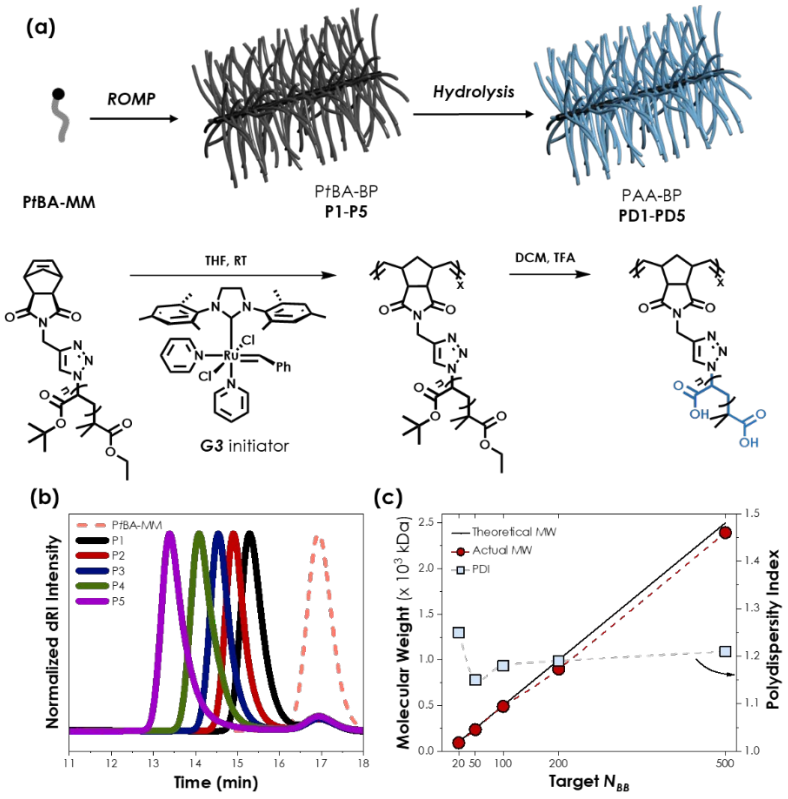

Figure 1. (a) Schematic illustration of the ROMP of **P*t*BA-MM** and hydrolysis; (b) MALLS-SEC traces of **P*t*BA-BPs**; (c) ROMP results of molecular weight and polydispersity index with targeted N_{BB} ([MM]/[initiator]).

Table 1. Characterization data for P*t*BA-BPs, **P1-P5**.

entry	Target N_{BB} ([MMs]/[G3])	$M_{n,\,theo}$[a] (kDa)	$M_{n,\,SEC}$[b] (kDa)	PDI[b]	Conversion[c] (%)
P1	20	100	91	1.25	96
P2	50	250	236	1.15	94
P3	100	500	490	1.18	95
P4	200	1,000	899	1.19	94
P5	500	2,500	2,393	1.21	95

a. Theoretical number-averaged molecular weights ($M_{n,theo}$) were calculated by [$M_{n,\,SEC}$ (**P*t*BA-MM**)] x [target N_{BB}].
b. $M_{n,\,SEC}$ and PDI were determined by MALLS-SEC.
c. Macromonomer conversions were approximated by comparing the dRI peak area between **P*t*BA-BP** and residual **P*t*BA-MM**.

Interfacial Aseembly of PAA-BP.

The PAA-BPs dissolved in water and polyhedral silsequioxane-NH_2 (POSS-NH_2) dispersed in toluene electrostatically interact at the interface to form BPSs (**Scheme 1**). Without POSS-NH_2, the interfacial activity of PAA-BPs is solely dictated by the degree of protonation of carboxylates at a fixed BP concentration. The interfacial activity of the PAA bottlebrush polymers (w/o POSS-NH_2) as a function of pH was assessed by pendant drop tensiometry by injecting a 5 μL water droplet ([**PD1**] = 1 mg mL^{-1}) into a pure toluene solution (**Figure S20a**). As the pH of the aqueous **PD1** solution increased from 2.4 to 7.2, the equilibrium interfacial tension (γ) increased from 16 to 31 mN m^{-1}, respectively, (**Figure S20c**), due to the decreased amphiphilicity associated with carboxylate ion formation. Upon reduction of droplet volume, wrinkles were not observed at the water/toluene interface regardless of pH, demonstrating the weak binding energy of BPs at fluid interfaces. For the highest MW case, **PD5**, the polymers precipitated when the pH decreased to 2.5, consequently, the pH of each polymer solution was set to 2.8-2.9. Other control experiments (*e.g.*, the effect of N_{BB} of PAA-BP without POSS-NH_2 in toluene, the effect of either pH of water or [**PD1**] with POSS-NH_2 in toluene, and [POSS-NH_2] of toluene with water with **PD1**) are summarized in supporting information (**Figure S20d-e**, **Figure S21a-g**).

The N_{BB}-dependence of the interfacial activity was determined by injecting 5 μL of an aqueous solution of PAA-BPs ([BPs]=1 mg mL^{-1}, pH~2.8) to form a droplet in a 0.1 mg ml^{-1} toluene solution of the POSS-NH_2 ($\gamma_{\text{pure water-pure toluene}}$~35 mN m^{-1}). **Figure 2a** highlights the PAA/POSS-NH_2 interactions at the fluid interface. The initial interfacial tension of the fluid interface was 6-8 mN m^{-1}, regardless of the N_{BB} of the BPs, reflecting the rapid adsorption and formation of the BPSs even before the first data point could be collected. The initial interfacial tensions of all the BPs were similar, indicating a similar number of 'mers' initially adsorbed to the fluid interface. Further reduction of γ requires the formation of additional BPSs at the interface. Since POSS-NH_2 is interfacially active[11], the formation of additional BPSs would be dictated by the diffusion of additional PAA-BPs to the interface along with a reorganization of the BPSs already assembled on the interface to accommodate the newly arrived PAA-BPs. One would anticipate that γ of the lower N_{BB} polymers (*e.g.*, **PD1**) would decrease more rapidly than that for the higher N_{BB} polymers (*e.g.*, **PD5**). This, however, is not the case with the highest MW polymer (**PD5**) showing the most rapid reduction in γ ($\Delta\gamma/\Delta t$, see **Figure S23a**), with $\Delta\gamma/\Delta t$ decreasing with decreasing N_{BB} of the BP (**Figure S23a**). At this PAA-BP concentration ([BP] = 1 mg mL^{-1}), BP

diffusion is not rate limiting but rather the number of functional groups (here, carboxylic acid) per BP, which is proportional to N_{BB}. Once any part of the BPs encounters the interface and interacts with POSS-NH_2, the remaining portions of the polymers are rapidly drawn to the interface to maximize interactions with the POSS-NH_2 and minimize γ. These results also suggest that the chain end of the BPs (high or low molecular weight) encounters the interface first with the remaining length of the molecule being rapidly anchored onto the interface. For both the low and high molecular weight BPs, this requires essentially the advance of a line through the already assembled BPSs and the energetic gain, per molecule, increases rapidly with molecular weight.

The equilibrium γ (**Figure 2c**) increased from 2.3 to 3 mN m^{-1} as N_{BB} increased from 20 to 100, since the effective area projected by the molecule changes from spherical to ellipsoid, reducing the packing efficiency of the BPSs at the fluid interface. However, when N_{BB} increased from 100 to 500, a decrease in γ was observed. To explain the two different trends in the equilibrium γ with N_{BB}, one needs to know parameters (e.g., shape, flexibility) associated with the conformation of BPs in solution. Sing and coworkers studied the conformation of bottlebrush polymer in solution with different N_{BB} or N_{SC}. In their work, they found that the conformation of bottlebrush polymers (N_{SC}=30, N_{BB}=21 to 87, $N_{BB} \leq N_{SC}$ regime) in solution changed from a spherical to a rod-like cylinder (rigid). When N_{BB} increased further to 175 and 703 ($N_{BB} >> N_{SC}$ regime), the macromolecule became more worm-like (semi-flexible) in character.[36] In our system, the PAA-BP became much more flexible when N_{BB} increased to 500 (N_{SC}~37, based on the ^{1}H NMR peak integration result, **Figure S7**), allowing them to anchor at the fluid interface at multiple sites, decreasing the equilibrium γ.

The packing efficiency of NPs is important for successful liquid printing, which would be related to the size or shape of NPs. In our case, the shape of the PAA-BPs changes depending on the $N_{BB} \sim N_{SC}$ ratio, which can affect their interfacial packing. In this regard, the apparent surface coverage (ASC), defined by the ratio of the droplet interfacial area when wrinkles are first observed (S_w) upon volume reduction (hence interfacial area reduction) to the initial interfacial area of the water droplet (S_0), was used to characterize the packing efficiency of PAA-BPs. As shown **Figures 2d** and **2e,** the ASC for an aqueous **PD1** droplet was found to be 0.95, where wrinkling was observed almost immediately upon reducing the interfacial area. For the higher molecular weight **PD5,** the volume of the droplets was decreased further to generate a well-defined PAA/POSS-NH_2 film and a wrinkle pattern on the droplet surface, giving a lower ASC of 0.72. Upon further

reduction in the molecular weight, the film formed with **PD1** (**Figure 2d (ii)**) did not show any relaxation of the wrinkles, even after aging for 12 hours (**Figure 2d (iii)**). However, for **PD5** (**Figure 2e (ii)**), the wrinkles relaxed immediately (**Figure 2e (iii)**). During the relaxation, the large decrease in γ caused the droplet to fall from the needle. The monotonic decreasing trend in the ASC with MW shown in **Figure 2c** and the stress relaxation behavior for different N_{BB} BPs indicate that the molecular packing and, hence, the degree of reorganization of the assembled BPSs depended on macromolecular topology. That the ASC of linear PAA is low (ASC~28 %, aging 10 hours even after IFT reached equilibrium, **Figure S24**) compared to **PD1**, despite their similar MW (~50 kDa), underscores the importance of macromolecular topology on the jamming behavior.

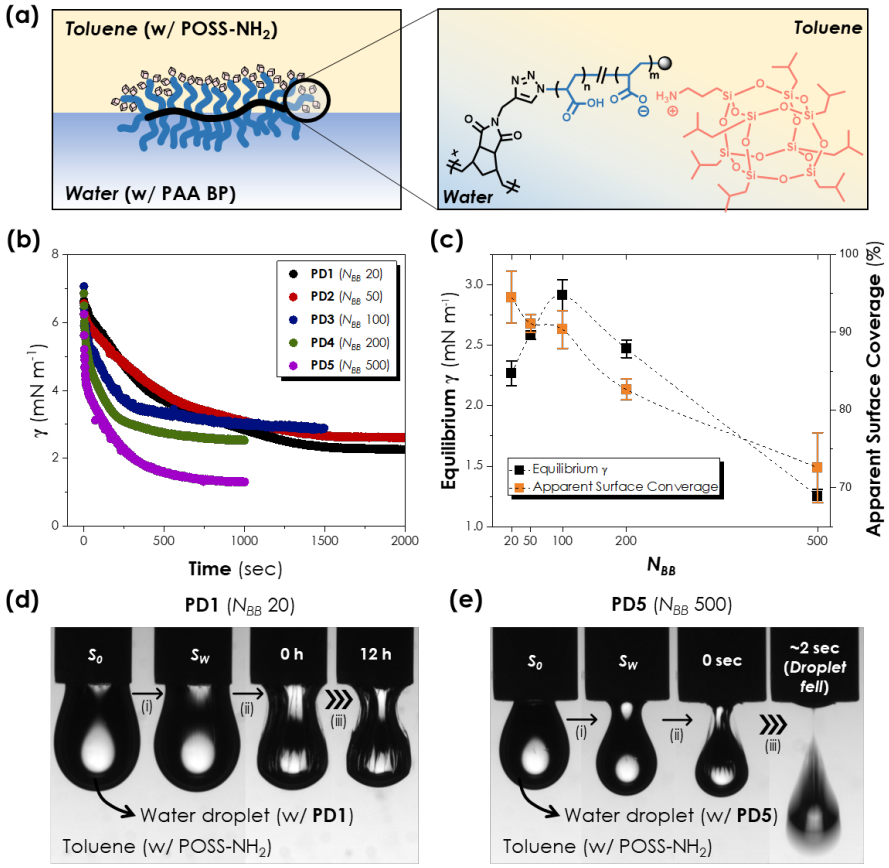

Figure 2. (a) Schematic illustration of PAA-BPs/POSS-NH_2 complexation at water/toluene interface via electrostatic interaction. (b) Time dependence of interfacial tension at water/toluene interface for different N_{BB} (water phase, [BPs] = 1 mg mL^{-1}, pH 2.8) with POSS-NH_2 (toluene phase, 0.1 mg mL^{-1}). (c) Equilibrium interfacial tension and apparent surface coverage of BPSs as a function of N_{BB}. Snapshots of water droplet containing (d) **PD1** and (e) **PD5** ([BPs] = 1 mg mL^{-1}, pH 2.8) in toluene ([POSS-NH_2] = 0.1 mg mL^{-1}). The initial interfacial area (S_0) upon approaching equilibrium interfacial tension.

Kinetics of Interfacial Assembly

Suppressing the Plateau-Rayleigh instability, dictating whether the liquid drips or jets, is essential for all-liquid printing and is directly related to γ of liquid interfaces, the jetting rate, and the viscosity of the surrounding liquid (**Figure 3a**). **Figure S21b-e** show that high [POSS-NH_2] and low pH of water containing BPs yielded a lower initial γ. These results match well with the dripping-to-jetting transition as a function of increasing [POSS-NH_2] and decreasing pH of the aqueous phase shown in **Figure 3b** and **c**. By varying N_{BB} of BPs, the dependence of the initial interfacial assembly kinetics on the MW of polymer (**Figure 3d**) was assessed. At a flow rate of 0.6 mL min^{-1}, only **PD5** showed a dripping-to-jetting transition, but, at flow rates of 1.2 and 1.5 mL min^{-1} only **PD1** showed a dripping-to-jetting transition, demonstrating the faster initial interfacial assembly of higher N_{BB} PAA-BPs.

The initial assembly kinetics for two representative N_{BB} values (20 and 500) were investigated by fluorescence recovery after photobleaching (FRAP). The synthesis of PAA-BPs containing 0.5 mole % Rhodamine B (**Figure 5e**) is detailed in the Supporting Information (**Figure S13-16**, **18**, and **Table S2-4**). Fresh emulsions with **PD6** (N_{BB} 20 with dye) and **PD7** (N_{BB} 500 with dye) showed marked differences of the fluorescence intensity recovery. For **PD6**, the intensity of the bleached area recovered to 0.6 (normalized intensity, I/I_0), indicating that the fluid interface was not fully covered by the BPSs (**Figure 3f**). The intensity, however, did not recover to the same extent after aging the emulsion for 24 hours (**Figure 3f**), due to the high surface coverage that restricts *in-plane* diffusion (reorganization). Emulsions based on **PD7** showed negligible recovery for the fresh emulsion, caused by the rapid initial interfacial assembly (**Figure 3g**). Overall, both the jetting and FRAP experiments demonstrated that BPs with high N_{BB} assembled at the fluid interface much more rapidly than those with low N_{BB} (*vide supra*).

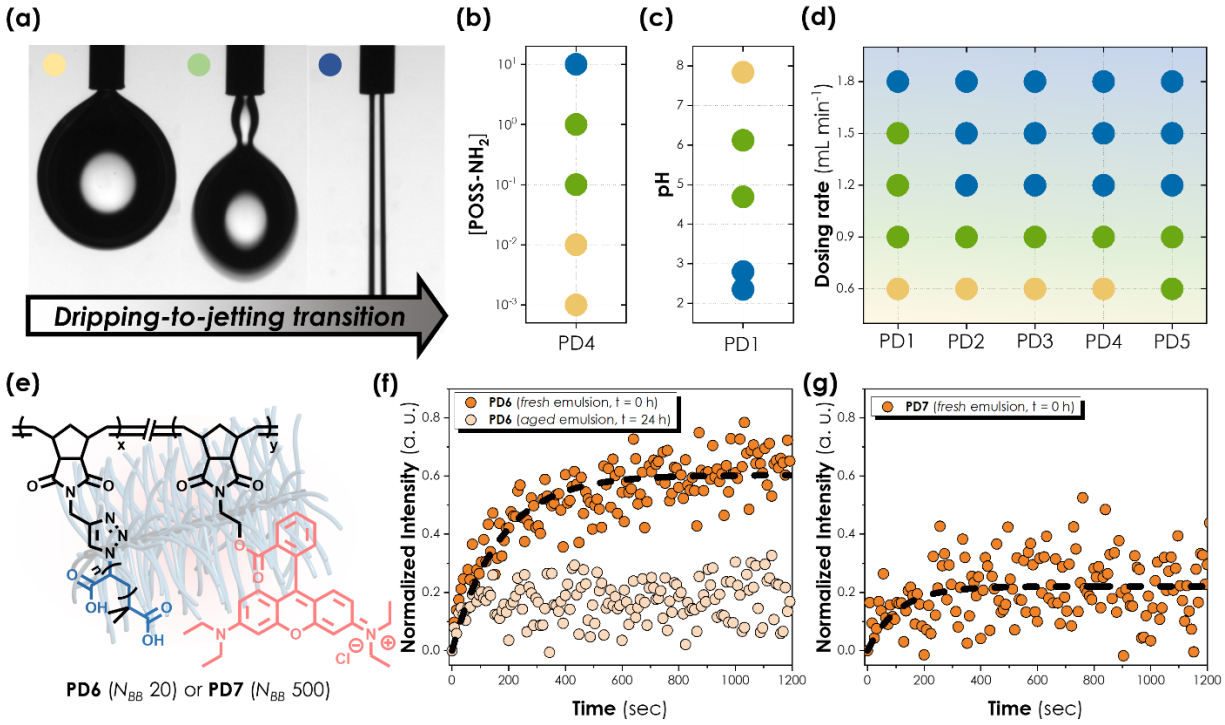

Figure 3. Water phase ([BPs] = 1 mg mL^{-1}, pH 2.8) injection in toluene ([POSS-NH$_2$] = 10 mg mL^{-1}). (a) Representative dripping (left droplet, yellow dot), dripping-to-jetting transition (middle droplet, green dot), and jetting (right water stream, blue dot) regimes. (b) Effect of [POSS-NH$_2$] in toluene with **PD4** (1 mg mL^{-1}, pH 2.8), (c) effect of pH of water phase ([**PD1**] = 1 mg mL^{-1}), and (d) effect of N_{BB} of BPs in water ([BPs] = 1 mg mL^{-1}, pH 2.8) by injecting water phase in toluene ([POSS-NH$_2$] = 10 mg mL^{-1}). (e) Schematic illustration of **PD6** (N_{BB} 20) and **PD7** (N_{BB} 500), containing NB-RB (0.5 mol %). FRAP results for (f) **PD6** (N_{BB} 20) with two different time frame (orange dots for FRAP result of fresh emulsion and beige dots for FRAP result of aged emulsion) and (g) **PD7** (N_{BB} 500) with FRAP result of fresh emulsion (orange dots).

Mechanical Properties of Assemblies

The mechanical properties of the structured liquids, *e.g.*, bending modulus or stress relaxation after compression, depends on the NP size, shape and concentration of the NPSs and the nature of the hydrophobic polymer ligands (number/distribution of complementary functional groups along the ligand).[37] Marked differences in the relaxation of wrinkles with different N_{BB} (**Figure 2d** and **e**) led us to quantify the stress relaxation and bending modulus of BPSs with different N_{BB}. The different wavelengths of the sinusoidal wrinkle patterns and the relaxation behavior from **PD1** to **PD5** demonstrate that the BPSs have different mechanical properties with different N_{BB}. The wrinkling patterns of BPSs with 5 different N_{BB} were obtained by using a Langmuir trough as follows: (i) a toluene solution of POSS-NH$_2$ ([POSS-NH$_2$] = 0.6 mg mL^{-1}) was placed on top of an aqueous PAA-BP solution ([BPs] = 0.05 mg mL^{-1}, pH 2.9), (ii) the interfacial assembly was allowed to equilibrate (***T$_0$***, Stage 1, **Figure 4b**) , (iii) a barrier was used

to reduce interfacial area to induce a wrinkling of the assembly (***T1***, Stage 2, **Figure 4b**), (iv) the wrinkle patterns were recorded, and the wavelength (λ) and the amplitude (A) of the wrinkles were determined by image analysis (MATLAB®). Detailed descriptions of the procedures are provided in the Supporting Information. The lower N_{BB} BP showed more regular wrinkle patterns than those of higher N_{BB} (***T1***, **Figure 4a**). The stress relaxation behavior as a function of time for different N_{BB} was described by:

$$\frac{\langle\sigma\rangle}{\langle\sigma_0\rangle} \approx \sqrt{\frac{I}{I_0}}\frac{\lambda}{\lambda_0}$$

where $\langle\sigma\rangle$ is normalized stress, $\langle\sigma_0\rangle$ is normalized initial stress and I is the intensity. The time-dependent normalized stress ($\langle\sigma\rangle\ \langle\sigma_0\rangle^{-1}$) in **Figure 4d** shows a dependence on N_{BB}. As N_{BB} increased, a more rapid initial stress relaxation ($\partial[\langle\sigma\rangle\ \langle\sigma_0\rangle^{-1}]/\ \partial t_{t\to 0}$) and a higher degree of stress relaxation ($|\Delta(\langle\sigma\rangle\ \langle\sigma_0\rangle^{-1})|$) were observed. From the time-dependent normalized stress (**Figure 4d**), the characteristic stress relaxation time (τ_{SR}) was determined by fitting to:

$$\frac{\langle\sigma\rangle}{\langle\sigma_0\rangle} = A + Be^{-\left(\frac{t}{\tau_{SR}}\right)\beta}$$

In **Figure 4e**, τ_{SR} shows two different regimes, one that decreased with N_{BB} (from 20 to 100), and another that showed negligible changes with N_{BB} (from 100 to 500). As discussed earlier, significant changes in the effective shape of the assembled BPs projected onto fluid interfaces occurs in the regime from $N_{BB} \leq N_{SC}$ (spherical) to $N_{BB} > N_{SC}$ (cylindrical). Since for BP N_{SC}~37, the spherical-to-cylindrical transition occurs when N_{BB}~37, therefore **PD2** falls into this transition regime. As the BP shape changes from spherical (**PD1**)-to-cylindrical (**PD3**), a significant decrease in the packing efficiency is expected, leading to a more rapid stress relaxation by a reorganization upon jamming. Even though the τ_{SR} has similar values for **PD3** to **PD5**, the equilibrium $\langle\sigma\rangle\ \langle\sigma_0\rangle^{-1}$ decreases from 0.5 (**PD3**) to 0.3 (**PD5**), showing the importance of packing efficiency on the stress relaxation. The wavelength of the buckling pattern is related to the bending modulus (B) of the NPSs by:

$$\lambda = 2\pi\left(\frac{B}{\Delta\rho g}\right)^{1/4}$$

where Δρ is density difference between the two liquid phases (0.13 g mL^{-1}) and g is gravitational acceleration (9.8 m^2 sec^{-1}).[8, 37] Since the resulting wrinkle patterns gave a distribution of wavelengths, we took a mean wavelength ($\bar{\lambda}$) and used this to determine B. Initially B decreases

with N_{BB} (from 2x10^3 k_BT for **PD1** to 3x10^2 k_BT for **PD3**), reaches a minimum at N_{BB} = 100 (**PD3**), and then increases with N_{BB} (5x10^3 k_BT for **PD5**, **Figure 4f**). The bending modulus for spherical hard nanoparticles showed a single value with time[8], however, in the case of the BPSs system, the wavelengths of wrinkles changed with time for all BPs, caused by the molecular reorganization upon compression, due to the particle shape and soft nature of the BPSs. As discussed earlier in **Figure 2c**, a decrease in the ASC with increasing N_{BB} was found. As the N_{BB} increased further (100 to 500), however, the individual BPs became semi-flexible in solution[36], allowing them to form PAA/POSS-NH_2 complexes at multiple sites at fluid interfaces. As B is determined by both Young's modulus and structure of the NPSs, if the NPSs form a monolayer, then the resistance towards bending of the individual NP affects B.[8] Since BPSs with higher N_{BB} form PAA/POSS-NH_2 complexes at multiple sites, when the BPSs are compressed, the tension caused by compression along the backbone of individual BP contributes the macroscopic bending rigidity, and hence higher B (**Figure 4f**).

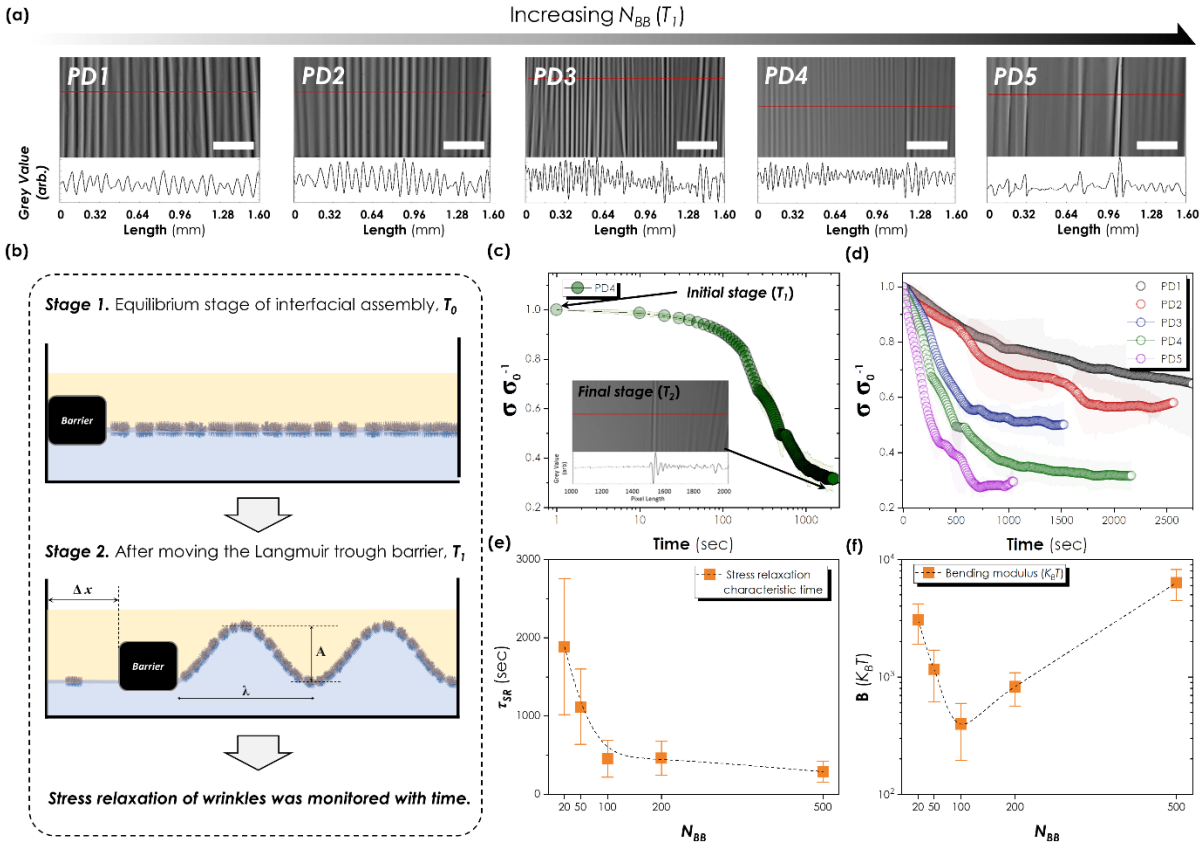

Figure 4. Bending modulus and stress relaxation behavior of the BPSs with different N_{BB}. (a) Optical micrographs of bottlebrush polymer surfactant assemblies with different N_{BB}. Scale bar = 300 μm. (b) Schematic illustration of

buckling formation by moving the barrier (Δx) of Langmuir trough. (c) Stress relaxation of **PD4**-POSS complex with semi-log plot and (d) different N_{BB} of BP-POSS complex with linear plot. (e) Stress relaxation characteristic time and (f) bending modulus as a function of N_{BB}.

Stability of All-Liquids Printed Constructs

The N_{BB} dependence of the BP assembly dynamics and BPS mechanical properties at the fluid interfaces gave rise to the use of BPSs for all-liquid printing. **Figure 5a** shows a brief schematic illustration on the liquid-in-liquid printing with a 3D printer and BPS formation at the water/silicone oil interfaces. To judge the stability of the printed liquids, a spiral geometry of an aqueous phase (either **PD1** or **PD5**, [BPs] = 10 mg mL^{-1}, pH 2.8) was jetted (flow rate=0.5 mL min^{-1}) into a silicone oil (η = 10,000 cSt) with *bis*-3-aminopropyl terminated poly(dimethylsiloxane) (H_2N-PDMS-NH_2, 3 kDa, 5 volume % in oil) (**Figure 5b**). For **PD1** and **PD5**, the initial liquid spirals were stable and retained their original printed structure. However, degradation of both the inner and outer sections of the spiral were observed for **PD5** after 5 minutes. Only a slight degradation of inner section of the spiral was observed for **PD1**. This difference became clearer after aging for 2 hours, where the printed structure degraded into droplets for **PD5**, but that for the **PD1** retained its original printed structure. Since the packing density of the BPSs with lower N_{BB} was higher than that of the higher N_{BB} BPs (**Figure 2c**), the BPS reorganization was significantly restricted, which provided more structural stability. When **PD1** and **PD5** were mixed by 1:1 mass ratio (molar ratio → **PD1**: **PD5** = 26.3 : 1) and printed in the same printing medium, an unstable liquid spiral was observed, showing that the mobility of BPSs was increased by the mixture of the BPs.

Figure 5c shows the dependence of the stability of the structured liquids on the ligand (PDMS-$(NH_2)_n$) size and the number of primary amine groups per PDMS chain. When the MW of H_2N-PDMS-NH_2 increased in a fixed volume % in silicone oil, two changes are expected: an increased inter-BP crosslinking and a decreased concentration of amine groups in the oil phase. For a fixed volume % in silicone oil, changing the size of PDMS from 3 kDa (**Figure 5b**, **PD5** case) to 1 kDa increases the concentration of amine groups in the medium by a factor of 3, enabling more electrostatic interactions with the BPs and, hence, an enhanced binding energy of the BPSs. However, inter-BP crosslinking, due to connectivity or crosslinking between two different BPs, decreases for the lower molecular weight PDMS, which affects the macroscopic stability of the printed liquid. Upon printing a spiral with 1 kDa H_2N-PDMS-NH_2, spherical water droplets formed

immediately, due to the lower stability of the printed liquids caused by a decreased inter-BP crosslinking, and the structure fully degraded into droplets within 10 minutes (**Figure 5c**, upper row). More efficient crosslinking between BPs is expected by increasing H_2N-PDMS-NH_2 MW to 25 kDa (**Figure 5c**, middle row); however, the structured liquid was unstable upon printing and degraded into droplets within 1 minute. In this case, the number of amine groups in the silicone oil decreased by a factor of 8 in comparison to the 3 kDa case (**Figure 5b**, middle row), indicating a deficiency of amine groups to hold BPs efficiently at the liquid interface upon compression. Lastly, if the PDMS has multiple amine groups along the PDMS chain, an enhanced stability of the printed structures would be expected with long backbones of BP. Even 120 minutes after printing the construct remained in its original trajectory with the multi-amine-functionalized PDMS (20 kDa, 2-3 mol % amine per chain, **Figure 5c**, lower row).

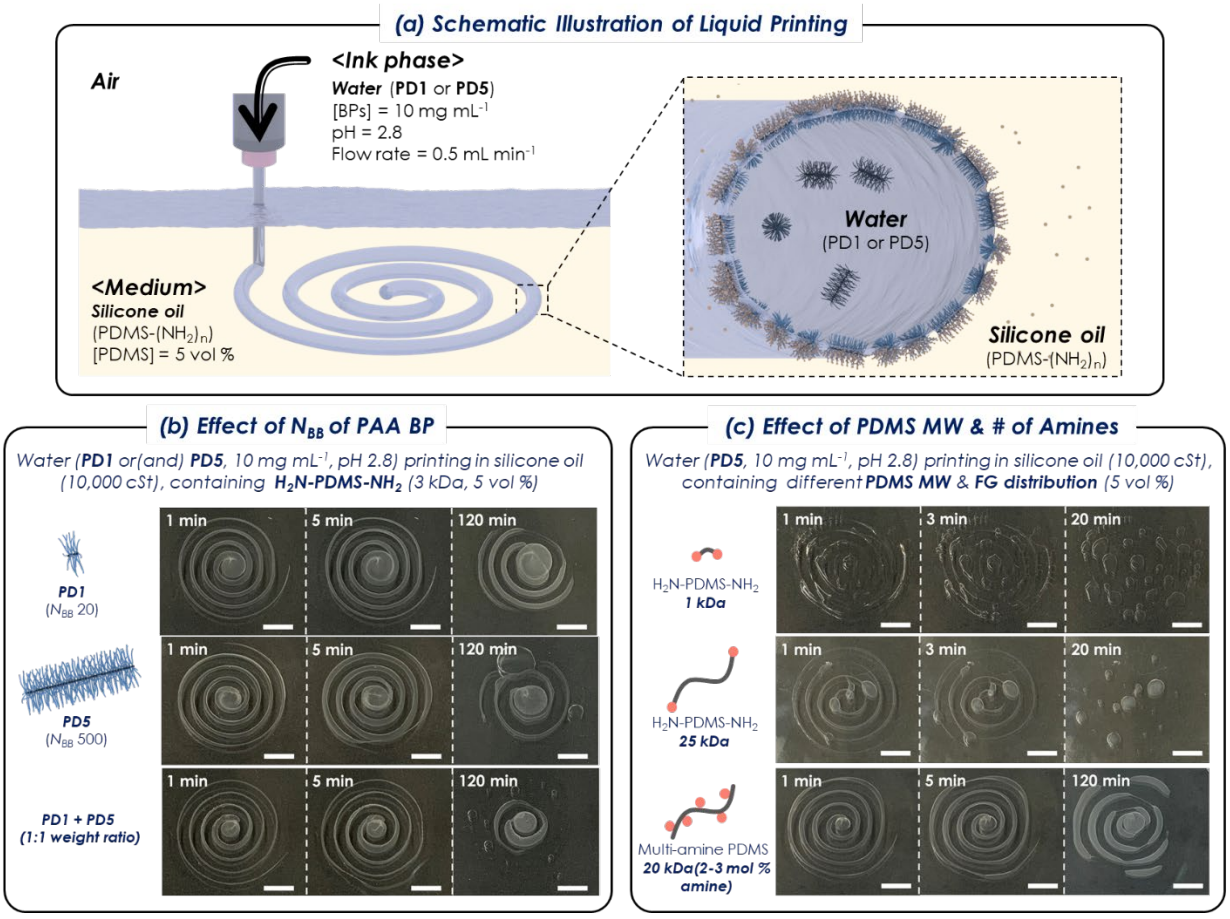

Figure 5. (a)Schematic illustration of 3D printing of all-liquids constructs by formation of carboxylate-ammonium complexation at the fluid interface. (a) Effect of N_{BB} (20, 500, or mixture) on stability of printed spirals and (b) effect of size (1 to 25 kDa) or amine mol % of polymeric ligands (bis-3-aminopropyl terminated or multi-amine-functionalized PDMS) in oil. Scale bar = 1 cm.

CONCLUSION.

In summary, we described the N_{BB}-dependent bottlebrush polymer surfactants assembly kinetics, packing efficiency, and mechanical properties (bending rigidity as well as stress relaxation behavior upon compression of the BPSs assembly). The N_{BB}~N_{SC} ratio, which changes the effective area of the BPs projected onto fluid interfaces of the polymer from spherical ($N_{BB}\leq N_{SC}$) to cylinder ($N_{BB}>N_{SC}$). In $N_{BB}\leq N_{SC}$, was found to be key in increasing γ_{eq} and decreasing B, due to a shape transformation of the dissolved polymer. However, for $N_{BB}>N_{SC}$, the flexibility of the polymer chain along the backbone increases, decreasing γ_{eq} and increasing B by the multi-sites anchoring of the BPs. *The faster interfacial assembly at early-stage (larger $-\partial\gamma/\partial t$) and high B for $N_{BB}>N_{SC}$ are beneficial for successful liquids printing, however, BPs with $N_{BB}\leq N_{SC}$ gives densely packed BPSs (high ASC), which in turn gives a higher B and a decrease in the degree of stress relaxation, yielding more stable structured liquids*. The results shown here provide a general design rule for the printing of structured liquids using bottlebrush polymers. Owing to the high density of functional groups at the printed liquid interface of the BPSs, interfacial chemistries for applications, such as biphasic reactors, by incorporating metal cations or active enzymes are possible.

Acknowledgements

This work was supported by the U.S. Department of Energy, Office of Science, Office of Basic Energy Sciences, Materials Sciences and Engineering Division under Contract No. DE-AC02-05-CH11231 within the Adaptive Interfacial Assemblies Towards Structuring Liquids program (KCTR16) and by the Army Research Office under contract W911NF-20-0093.

References

1. Pickering, S. U., Emulsions. *Journal of the Chemical Society, Transactions* **1907,** *91*, 2001-2021.

2. Binks, B. P., Particles as surfactants-similarities and differences. *Current Opinion in Colloid & Interface Science* **2002,** *7* (1-2), 21-41.

3. Boker, A.; He, J.; Emrick, T.; Russell, T. P., Self-assembly of nanoparticles at interfaces. *Soft Matter* **2007,** *3* (10), 1231-1248.

4. Pieranski, P., Two-Dimensional Interfacial Colloidal Crystals. *Phys. Rev. Lett.* **1980,** *45* (7), 569-572.

5. Wu, J.; Ma, G. H., Recent Studies of Pickering Emulsions: Particles Make the Difference. *Small* **2016,** *12* (34), 4633-48.

6. Lin, Y.; Skaff, H.; Emrick, T.; Dinsmore, A. D.; Russell, T. P., Nanoparticle Assembly and Transport at Liquid-Liquid Interfaces. *Science* **2003,** *299*, 226-229.

7. Cui, M.; Emrick, T.; Russell, T. P., Stabilizing Liquid Drops in Nonequilibrium Shapes by the Interfacial Jamming of Nanoparticles. *Science* **2013,** *342* (6157), 460-463.

8. Leahy, B. D.; Pocivavsek, L.; Meron, M.; Lam, K. L.; Salas, D.; Viccaro, P. J.; Lee, K. Y.; Lin, B., Geometric stability and elastic response of a supported nanoparticle film. *Phys. Rev. Lett.* **2010,** *105* (5), 058301.

9. Xie, G.; Forth, J.; Chai, Y.; Ashby, P. D.; Helms, B. A.; Russell, T. P., Compartmentalized, All-Aqueous Flow-Through-Coordinated Reaction Systems. *Chem* **2019,** *5* (10), 2678-2690.

10. Liu, X.; Kent, N.; Ceballos, A.; Streubel, R.; Jiang, Y.; Chai, Y.; Kim, P. Y.; Forth, J.; Hellman, F.; Shi, S.; Wang, D.; Helms, B. A.; Ashby, P. D.; Fischer, P.; Russell, T. P., Reconfigurable ferromagnetic liquid droplets. *Science* **2019,** *365* (6450), 264-267.

11. Hou, H.; Li, J.; Li, X.; Forth, J.; Yin, J.; Jiang, X.; Helms, B. A.; Russell, T. P., Interfacial Activity of Amine-Functionalized Polyhedral Oligomeric Silsesquioxanes (POSS): A Simple Strategy To Structure Liquids. *Angew. Chem. Int. Ed. Engl* **2019,** *58* (30), 10142-10147.

12. Feng, T.; Hoagland, D. A.; Russell, T. P., Assembly of acid-functionalized single-walled carbon nanotubes at oil/water interfaces. *Langmuir* **2014,** *30* (4), 1072-1079.

13. He, J.; Zhang, Q.; Gupta, S.; Emrick, T.; Russell, T. P.; Thiyagarajan, P., Drying droplets: a window into the behavior of nanorods at interfaces. *Small* **2007,** *3* (7), 1214-1217.

14. Liu, X.; Shi, S.; Li, Y.; Forth, J.; Wang, D.; Russell, T. P., Liquid Tubule Formation and Stabilization Using Cellulose Nanocrystal Surfactants. *Angew. Chem. Int. Ed. Engl* **2017,** *56* (41), 12594-12598.

15. Wang, B.; Liu, T.; Chen, H.; Yin, B.; Zhang, Z.; Russell, T. P.; Shi, S., Molecular Brush Surfactants: Versatile Emulsifiers for Stabilizing and Structuring Liquids. *Angew. Chem. Int. Ed. Engl* **2021,** *60* (36), 19626-19630.

16. Sun, Z.; Feng, T.; Russell, T. P., Assembly of graphene oxide at water/oil interfaces: tessellated nanotiles. *Langmuir* **2013,** *29* (44), 13407-13413.

17. Cain, J. D.; Azizi, A.; Maleski, K.; Anasori, B.; Glazer, E. C.; Kim, P. Y.; Gogotsi, Y.; Helms, B. A.; Russell, T. P.; Zettl, A., Sculpting Liquids with Two-Dimensional Materials: The Assembly of Ti(3)C(2)T(x) MXene Sheets at Liquid-Liquid Interfaces. *ACS Nano* **2019,** *13* (11), 12385-12392.

18. Qu, M.; Hou, J.; Liang, T.; Xiao, L.; Yang, J.; Raj, I.; Shao, Y., Preparation and Interfacial Properties of Ultralow Concentrations of Amphiphilic Molybdenum Disulfide Nanosheets. *Industrial & Engineering Chemistry Research* **2020,** *59* (19), 9066-9075.

19. Huang, C.; Sun, Z.; Cui, M.; Liu, F.; Helms, B. A.; Russell, T. P., Structured Liquids with pH-Triggered Reconfigurability. *Adv. Mater.* **2016,** *28* (31), 6612-6618.

20. Yin, Y.; Liu, T.; Wang, B.; Yin, B.; Yang, Y.; Russell, T. P.; Shi, S., Nanoparticle/Polyelectrolyte Complexes for Biomimetic Constructs. *Adv. Funct. Mater.* **2021,** *32* (6).

21. Sun, H.; Li, L.; Russell, T. P.; Shi, S., Photoresponsive Structured Liquids Enabled by Molecular Recognition at Liquid-Liquid Interfaces. *J. Am. Chem. Soc.* **2020,** *142* (19), 8591-8595.

22. Gu, P. Y.; Chai, Y.; Hou, H.; Xie, G.; Jiang, Y.; Xu, Q. F.; Liu, F.; Ashby, P. D.; Lu, J. M.; Russell, T. P., Stabilizing Liquids Using Interfacial Supramolecular Polymerization. *Angew. Chem. Int. Ed. Engl* **2019,** *58* (35), 12112-12116.

23. Sun, H.; Li, M.; Li, L.; Liu, T.; Luo, Y.; Russell, T. P.; Shi, S., Redox-Responsive, Reconfigurable All-Liquid Constructs. *J. Am. Chem. Soc.* **2021,** *143* (10), 3719-3722.

24. Hu, M.; Russell, T. P., Polymers with advanced architectures as emulsifiers for multi-functional emulsions. *Materials Chemistry Frontiers* **2021,** *5* (3), 1205-1220.

25. Walther, A.; Muller, A. H., Janus particles: synthesis, self-assembly, physical properties, and applications. *Chem. Rev.* **2013,** *113* (7), 5194-261.

26. Xie, G.; Krys, P.; Tilton, R. D.; Matyjaszewski, K., Heterografted Molecular Brushes as Stabilizers for Water-in-Oil Emulsions. *Macromolecules* **2017,** *50* (7), 2942-2950.

27. Ruhland, T. M.; Groschel, A. H.; Ballard, N.; Skelhon, T. S.; Walther, A.; Muller, A. H.; Bon, S. A., Influence of Janus particle shape on their interfacial behavior at liquid-liquid interfaces. *Langmuir* **2013,** *29* (5), 1388-94.

28. Jiang, Y.; Chakroun, R.; Gu, P.; Groschel, A. H.; Russell, T. P., Soft Polymer Janus Nanoparticles at Liquid-Liquid Interfaces. *Angew. Chem. Int. Ed. Engl* **2020,** *59* (31), 12751-12755.

29. Seong, H. -G.; Chen, Z.; Emrick, T.; Russell, T. P., Reconfiguration and Reorganization of Bottlebrush Polymer Surfactants. *Angew. Chem. Int. Ed. Engl* **2022,** *61* (19), e202200530.

30. Xia, Y.; Li, Y.; Burts, A. O.; Ottaviani, M. F.; Tirrell, D. A.; Johnson, J. A.; Turro, N. J.; Grubbs, R. H., EPR study of spin labeled brush polymers in organic solvents. *J. Am. Chem. Soc.* **2011,** *133* (49), 19953-9.

31. Sheiko, S. S.; Sumerlin, B. S.; Matyjaszewski, K., Cylindrical molecular brushes: Synthesis, characterization, and properties. *Prog. Polym. Sci.* **2008,** *33* (7), 759-785.

32. Forth, J.; Liu, X.; Hasnain, J.; Toor, A.; Miszta, K.; Shi, S.; Geissler, P. L.; Emrick, T.; Helms, B. A.; Russell, T. P., Reconfigurable Printed Liquids. *Adv. Mater.* **2018,** *30* (16), e1707603.

33. Utada, A. S.; Fernandez-Nieves, A.; Stone, H. A.; Weitz, D. A., Dripping to jetting transitions in coflowing liquid streams. *Phys. Rev. Lett.* **2007,** *99* (9), 094502.

34. Toor, A.; Helms, B. A.; Russell, T. P., Effect of Nanoparticle Surfactants on the Breakup of Free-Falling Water Jets during Continuous Processing of Reconfigurable Structured Liquid Droplets. *Nano Lett.* **2017,** *17* (5), 3119-3125.

35. Bates, C. M.; Chang, A. B.; Momčilović, N.; Jones, S. C.; Grubbs, R. H., ABA Triblock Brush Polymers: Synthesis, Self-Assembly, Conductivity, and Rheological Properties. *Macromolecules* **2015,** *48* (14), 4967-4973.

36. Dutta, S.; Wade, M. A.; Walsh, D. J.; Guironnet, D.; Rogers, S. A.; Sing, C. E., Dilute solution structure of bottlebrush polymers. *Soft Matter* **2019,** *15* (14), 2928-2941.

37. Forth, J.; Mariano, A.; Chai, Y.; Toor, A.; Hasnain, J.; Jiang, Y.; Feng, W.; Liu, X.; Geissler, P. L.; Menon, N.; Helms, B. A.; Ashby, P. D.; Russell, T. P., The Buckling Spectra of Nanoparticle Surfactant Assemblies. *Nano Lett.* **2021,** *21* (17), 7116-7122.